Properties of the $Ti_{40}Zr_{10}Cu_{36}Pd_{14}$ BMG Modified by Sn and Nb Additions

Anna Sypien, Mihail Stoica, and Tomasz Czeppe

The results of investigation of the influence of additions of 2 and 3 at.% of Sn and simultaneously of Sn and 3 at.% Nb on microstructure and properties of the bulk metallic glasses of composition $(Ti_{40}Cu_{36-x}Zr_{10}Pd_{14}Sn_x)_{100-y}Nb_y$ are reported. It was found that the additions of Sn increased the temperatures of glass transition (T_g), primary crystallization (T_x), melting, and liquidus as well as supercooled liquid range (ΔT) and glass forming ability (GFA). The nanohardness and elastic modulus decreased in alloys with 2 and 3 at.% Sn additions, revealing similar values. The 3 at.% Nb addition to the Sn-containing amorphous phase decreased as well all the T_g, T_x, T_L, and T_m temperatures as ΔT and GFA; however, relatively larger values of this parameters in alloys containing larger Sn content were preserved. In difference to the previously published results, in the case of the amorphous alloys containing small Nb and Sn additions, a noticeable amount of the quenched-in crystalline phases was not confirmed, at least of the micrometric sizes. In the case of the alloys containing Sn or both Sn and Nb, two slightly different amorphous phase compositions were detected, suggesting separation in the liquid phase. Phase composition of the alloys determined after amorphous phase crystallization was similar for all compositions. The phases Cu_8Zr_3, $CuTiZr$, and Pd_3Zr were mainly identified in the proportions dependent on the alloy compositions.

1. Introduction

Bulk metallic glasses, requiring relatively low critical cooling rates to form amorphous phase, remain very promising materials for some applications (Ref 1). In recent years, a lot of attention has been paid to exploring Ti-based crystalline alloys, characterized by high specific strength and low density. Another important property of the Ti alloys is their biocompatibility enabling applications in the field of medicine as different types of implants (Ref 2-4). Ti-based BMGs have potential to further expand into the medical application area, because of mechanical properties better fitting to the parameters required for the human implants than the crystalline alloys (Ref 5). Among different systems of multi-component glassy alloys, TiZrCuPd alloys were identified as potentially bio-compatible in spite of Cu content which remains cancerogenic in the human tissues (Ref 1, 5, 6). The $Ti_{40}Zr_{10}Cu_{40-x}Pd_{10+x}$ compositions with Pd content of 10, 14, and 20 at.% were first invented by Inoue group and later widely studied (Ref 7-9). These BMGs reveal quite large supercooled liquid range ΔT and glass forming ability (GFA). The amorphous phases reveal a complex, multi-stage crystallization process, good mechanical properties, and good corrosion resistance (Ref 7). Also, dL/L_0dT formability in the homogenous deformation range near T_g

Anna Sypien and **Tomasz Czeppe**, Institute of Metallurgy and Materials Sciences, Polish Academy of Sciences, Reymonta 25 St., 30-059 Kraków, Poland; and **Mihail Stoica**, Institute for Complex Materials, IFW Dresden, Helmholtzstr. 20, 01069 Dresden, Germany. Contact e-mail: a.sypien@imim.pl.

temperature is as large as $1.3 \cdot 10^{-4}$ $[T^{-1}]$ (Ref 10). Most of the investigations concentrated on the properties of the composition with 14 at.% of Pd because of the high GFA and large critical diameter of BMG available (Ref 5). To further increase the critical diameter of the bulk glassy samples preserving bio-compatibility, small amounts of Sn were added (Ref 5, 6), while Nb additions were used for the improvement in mechanical properties (Ref 11). As investigations of Zhu et al. (Ref 5, 6) have shown, $Ti_{40}Zr_{10}Cu_{36-x}Pd_{14}Sn_x$ alloys with additions of 2 and 4 at.% of Sn, could be fabricated as amorphous by the copper mold casting, with diameters up to 12 mm. However, 6 at.% addition of Sn lead to partially crystalline structure. In comparison with the $Ti_{40}Zr_{10}Cu_{36}Pd_{14}$ BMG, 2 and 4 at.% Sn additions caused an increase in T_g temperature and GFA, while the addition of 4 at.% Sn increased supercooled liquid range $\Delta T = T_x - T_g$. Except high strength in the range of 2000 MPa, the BMGs containing 2 at.% of Sn revealed large 3.5% plastic strain in relation to the branching of the shear bands (Ref 5). In the case of similar additions of Sn replacing components of the TiZrCuPd BMGs other than Cu, no improvement in GFA was noticed, except when Ti was replaced by 2 at.% of Sn. Also no increase in strength or plasticity was achieved (Ref 6).

The influence of the 1-5 at.% of Nb addition on the properties of $Ti_{40}Zr_{10}Cu_{36}Pd_{14}$ glassy alloy was investigated by Qin et al. (Ref 11). The Nb content increased both glass transition and primary crystallization temperatures T_g and T_x, but decreased GFA, which resulted in precipitation of the composition-dependent amount of the Pd_3Ti phase. This result agreed with the suggestion of Park et al. (Ref 12) that the addition of alloying element of Nb type may induce local structure heterogeneity in the amorphous matrix. Due to the crystalline nanoprecipitates, Nb-containing BMGs revealed increased yield strength above 2050 MPa, high Young modulus of about 80 GPa, and plastic strain of up to 8.5% (Ref 1). The Nb additions were also efficient in improving corrosion resistance and bio-compatibility of the bulk metallic glasses (Ref 13).

The mechanism of crystallization of all investigated amorphous alloys is quite complex, characterized by two or more exothermic effects on the DSC curves and may be modified by small additions of Sn and Nb (Ref 5, 6). The particles quenched in from the liquid phase or crystallizing in heating were identified as Cu_8Zr_3 and Cu_4Ti_3 (Ref 5) or Cu_8Zr_3, CuTi, and $PdTi_2$ (Ref 6). In the case of the amorphous alloy containing 2 at.% of Sn, the activation energy for primary crystallization increased to 334.3 kJ/mol from 287.6 for the $Ti_{40}Zr_{10}Cu_{36}Pd_{14}$ amorphous alloy (Ref 6). As shown in (Ref 14), in case of the $Ti_{40}Zr_{10}Cu_{40}Pd_{10}$ glassy alloy primary crystallization proceeded by diffusion of Ti and Cu between amorphous and crystalline phases, the last ones formed through the stage of 1-2 nm clusters growing to 5 nm crystallites identified as Cu_8Zr_3, Cu_2Ti, and Cu_3Pd phases.

In the present work, the influence of Sn and simultaneously Sn and Nb additions to the amorphous alloys of the composition $(Ti_{40}Cu_{36-x}Zr_{10}Pd_{14}Sn_x)_{100-y}Nb_y$, with $x = 2$, 3 and $y = 3$ on the glass microstructure, thermally induced crystallization process, and microhardness were investigated. As far as we know, the influence of such simultaneous additions of Sn, replacing Cu and Nb decreasing the content of all components, has not been reported yet.

2. Materials and Methods

The nominal composition of the investigated alloys named Pd-14, Sn-2, and Sn-3 was $Ti_{40}Cu_{36-x}Zr_{10}Pd_{14}Sn_x$ ($x = 0$, 2, 3 at.%), and for the alloys marked as Sn2Nb3 and Sn3Nb3 $(Ti_{40}Cu_{36-x}Zr_{10}Pd_{14}Sn_x)_{100-y}Nb_y$ ($y = 3$ at.%). The master alloys were prepared by cold crucible levitation melting under a high-purity argon atmosphere (Ref 15). The potentially amorphous bulk samples were prepared by the cooper mold injection casting method. The samples were 3 mm in diameter and 40 mm in length. The structure and phase composition of the alloys were determined with x-ray diffraction (XRD). The XRD equipment D2 Phaser (Brukers) with XFlash detector was used and Cu K_α radiation applied. The Rietveld method was used to calculate the amount of the main phases. After several attempts, the most suitable background and texture formulas were used. The microstructure was investigated with transmission (TEM), high resolution (HREM) and high-angle annular dark-field scanning transmission (HAADF-STEM) electron microscopy. The transmission electron microscope TECNAI (FEI, G2 FEG/200 kV) equipped with the EDAX Phoenix system for micro-analysis was used. The crystallization process was characterized by differential scanning calorimetry (DSC). The DSC experiments were performed in constant heating rate modes with rates from 10 to 30 K/min, with the use of the DuPoint 910 and F1 404 Netzsch DSC calorimeters. Glass transition temperature T_g was defined at the inflection point on the DSC curves. The nanohardness (NH_V) measurements may be used for monitoring the local change of microstructure and the corresponding mechanical properties. The UMIS indenter with Vickers diamond tip was used for such measurements. The applied load was 20 mN and at least 400 indentations were made in each case. The measurements with increasing penetration rates, 0.08 and 2.0 mN/s, were done with the 50 mN load, each time in six different places.

3. Results and Discussion

3.1 Amorphous Phase

The XRD patterns for the as-cast specimens shown in Fig. 1 are very similar, consisting mainly of one broad peak each. In the case of the Pd-14 and Sn-2 alloys, the diffraction patterns are typical of the fully amorphous alloys, while the XRD patterns for the Sn-3, Sn-2Nb-3, and Sn-3Nb-3 alloys contain a narrow intensity at the angle 2Θ of 40.5° suggesting melt-quenched crystalline particles.

The peak position fits the Cu_8Zr_3 phase (Table 2) which corresponds to phase identification in (Ref 6). Similarly, XRD pattern of the Sn-2Nb-3 sample contains a narrow peak at the angle of 41.45° suggesting participation of the nanocrystals in amorphous microstructure, probably ternary CuTiZr phase (Table 2).

The structure of the "as received" amorphous phase of the alloys containing Sn was further studied with the TEM and HAADF-STEM. Because the Sn-2 sample was completely amorphous, only TEM micrographs concerning Sn-3 massive sample which may contain crystalline particles are presented in Fig. 2.

As is visible in the bright-field (BF) (Fig. 2a) and dark-field (DF) (Fig. 2b) micrographs, no crystalline particles were detected. The SAED pattern (Fig. 2c) is also characteristic of the glassy phase. The composition-sensitive HAADF-STEM method was used as well (Fig. 3a, b). The STEM micrographs not only confirm differences in the foils' thickness visible in the BF micrograph but also reveal inhomogeneous composition in micro-volumes of the amorphous phase of the "island" and "valley" morphologies. The average composition of the islands in the case of the Sn-3 amorphous alloy was $Ti_{40}Cu_{30}Zr_{10}Pd_{17}Sn_3$ (points 2, 4 in Fig. 3a), showing an increase in the content of Pd by 3 at.%, compensated by the depletion in Cu in comparison with the nominal composition. The remaining components' content was unchanged. The separating valleys revealed the average composition $Ti_{30}Cu_{44}Zr_{15}Pd_8Sn_3$ (points 1, 3 in Fig. 3a), depleted in Ti (10 at.%) and Pd (6 at.%) and enriched in Cu and Zr. This result suggests melt separation into two slightly different compositions like $[(TiPd)_{50-x}(CuZr)_{50+x}]_{97}Sn_3$, probably also influencing thermal stability against crystallization. A similar result was achieved for the other amorphous alloys. As shown in Fig. 3b, for the Sn-2Nb-3 alloy the island composition agrees with the nominal composition, while the valleys are depleted in Ti and Pd and enriched in Cu and Zr, which confirms lack of the Nb influence on the component separation.

3.2 Thermally Induced Processes and Glass Forming Ability

The DSC curves corresponding to the glass transition and crystallization of the as-cast BMGs were measured at the constant heating rate of 30 °C/min and are shown in Fig. 4. The glass transition and primary crystallization temperature T_g and T_x as well as supercooled liquid temperature range $\Delta T = T_x - T_g$ are given in Table 1. All samples exhibit a clear endothermic heat event characteristic for glass transition, followed by the exothermic peaks resulting from the glass crystallization. The crystallization process consists of two or three peaks, revealing sensitivity to the small Sn and Sn+Nb additions and indicating complexity of the crystallization.
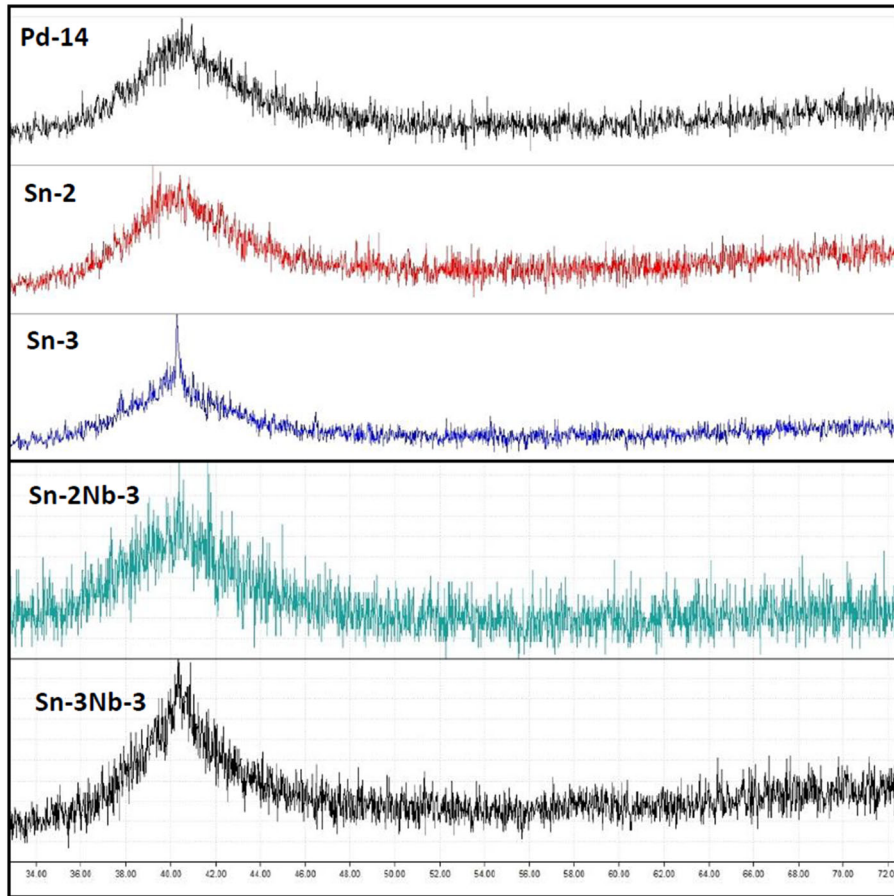
Fig. 1 XRD patterns of the amorphous alloys: (Pd-14) $Ti_{40}Cu_{36}Zr_{10}Pd_{14}$, (Sn-2) $Ti_{40}Cu_{34}Zr_{10}Pd_{14}Sn_2$, (Sn-3) $Ti_{40}Cu_{33}Zr_{10}Pd_{14}Sn_3$, (Sn-2Nb-3) $(Ti_{40}Cu_{34}Zr_{10}Pd_{14}Sn_2)_{97}Nb_3$, and (Sn-3Nb-3) $(Ti_{40}Cu_{33}Zr_{10}Pd_{14}Sn_3)_{97}Nb_3$
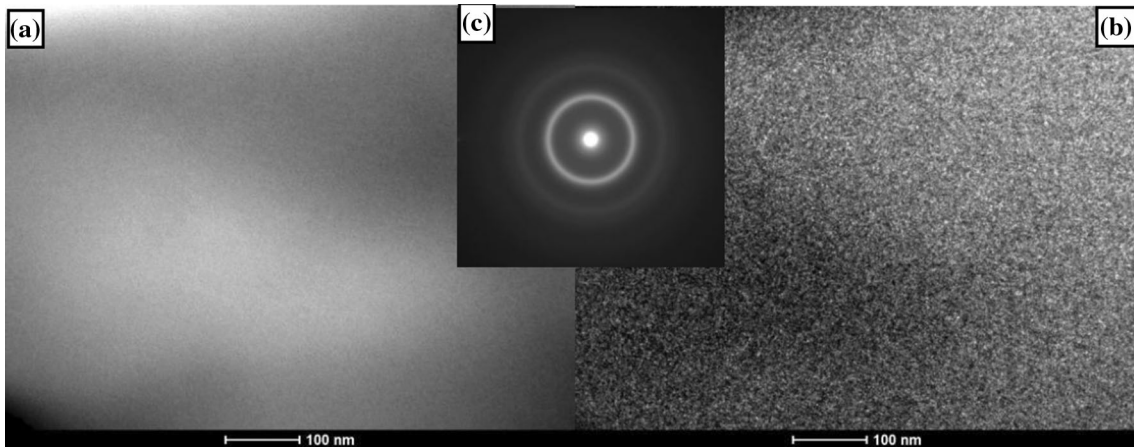

Fig. 2 TEM micrographs of Sn-3 BMG: (a) bright-field (BF), (b) dark-field (DF), and (c) selected area diffraction (SAED) pattern

As is visible from Table 1, as a result of the increase of Sn content to 3 at.%, glass transition temperature T_g increased by 9 °C, T_x temperature increased by 22 °C, and also supercooled liquid range ΔT increased by 12 °C. The 3 at.% addition of Nb generally decreased temperatures T_g and T_x and ΔT range but in different ways. T_g temperatures were decreased by about 5.5 °C in both Sn-2Nb-3 and Sn-3Nb-3 alloys, and T_x temperature was decreased by 11 °C in the case of Sn-2Nb-3 but only by 5 °C in case of the Sn-3Nb-3 alloy, preserving higher crystallization temperature T_x and the largest supercooled liquid temperature range for the alloys containing 3 at.% addition of Sn. As is also visible in Fig. 4, the 2 at.% Sn addition caused the third crystallization effect to appear at 578 °C in place of the single one. The 3 at.% Nb addition to this composition further
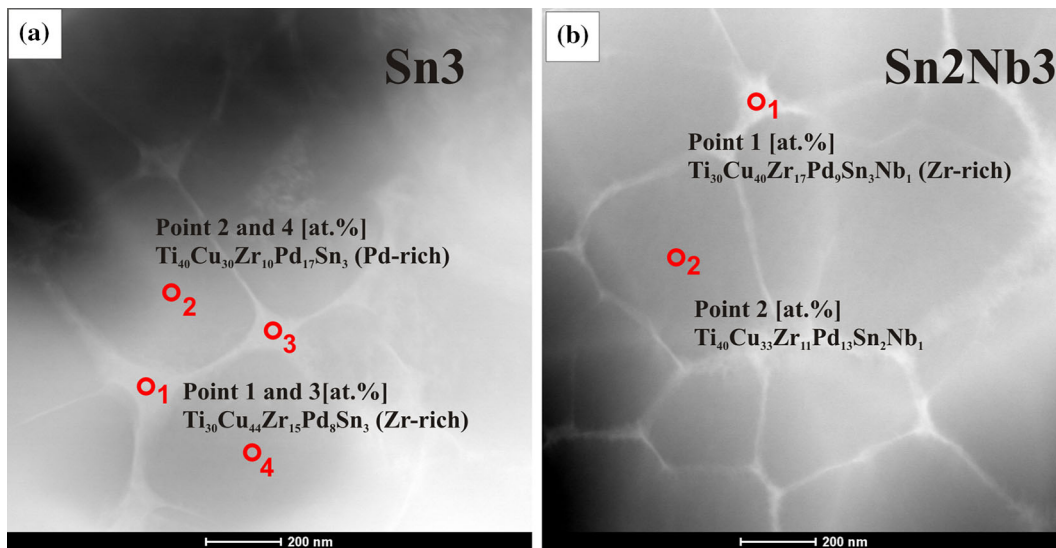
Fig. 3 TEM microstructure and (HAADF-STEM) image with marked points of the chemical composition analyses of (a) Sn-3 BMG and (b) Sn-2Nb-3 BMG
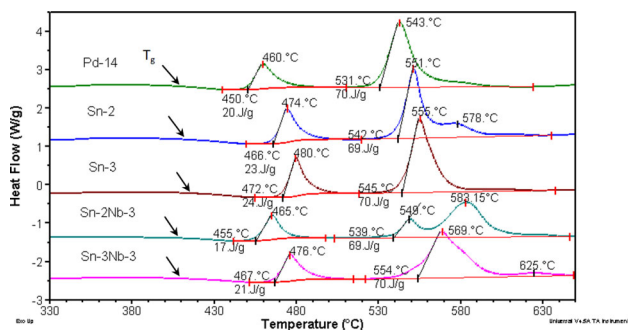

Fig. 4 Comparison of the DSC curves for the bulk amorphous samples of different compositions; heating rate 30 °C/min

increased this effect. However, the observation does not concern Sn-3 and Sn-3Nb-3 alloys revealing essentially single but widened secondary exothermic effects of crystallization. All these results show the independent and opposite influence of the Sn and Nb additions on the glass transition and the amorphous phase crystallization temperatures but a similar influence of the additions on the second step of the crystallization. It should be noted, however, that crystallization enthalpy was only slightly influenced at the primary crystallization step and remained independent of the number of further thermal events related to the crystallization (Fig. 4).

For the calculation of the GFA, the formula $T_{x1}/(T_{g}+T_{L})$ was used. The slower heating rate of 10 °C/min was used to determine melting and liquidus temperatures T_{m} and T_{L} of the alloys which are shown in Fig. 5 and summarized in Table 1. It is visible that the complex thermal effect of melting in case of the alloy Pd-14 Sn and Nb-less was replaced by one endothermic effect in alloys with Sn and Nb additions (Fig. 5; Table 1).

Similarly to the observations made for the crystallization process, an increase of the Sn content led to the increase in T_{m} and T_{L} temperatures, while the Nb addition did not significantly influence T_{m} temperature but decreased T_{L} temperature, also decreasing the $T_{L} - T_{m}$ temperature range (Table 1). As a

result, GFA increases with the increase of the Sn addition, and Nb addition decreases GFA but roughly proportionally to the values resulting from the Sn content.

3.3 Crystallization of the Amorphous Phase

TEM and HREM microstructures of the Sn-2 bulk sample annealed at T_{g} by 360 s are presented in Fig. 6 and 7, respectively. Both TEM micrographs and SAED pattern show nanocrystals in the amorphous phase together with large areas of a different, dark contrast. HREM micrograph in Fig. 7 confirms phase separation, as shown in Fig. 3. After annealing, the minor amorphous phase is not continuous as in Fig. 3 and partially remains still amorphous. The phase compositions of the alloys after the crystallization completed at 700 °C determined with XRD are shown in Fig. 8.

In that figure, the XRD patterns of the alloys with the 2 and 3 at.% of Sn are compared with those of the Pd-14 alloy and Nb-containing samples. As is clearly visible, the sequence of the main peaks does not change with the additions, suggesting crystallization of the same phases. However, while comparing the shape of the peaks it may be noticed that they are narrow in case of the Pd-14 sample and much broader in case of the Sn-2 and Sn-2Nb-3 samples. The broadening decreases further in case of the Sn-3 and Sn-3Nb-3 samples. This suggests that the crystallizing phases in case of the Sn as well as Sn and Nb additions are in dimensions of nanoparticles. Also the shape of the XRD intensity in case of the Sn-2 sample, in the 2θ angle from 36 to 46°, suggests that a large part of the amorphous phase was retained. This agrees well with the HREM microstructure presented in Fig. 7. An increase in the Sn and Nb content decreased this effect (Fig. 8). Phases giving the most intensive peaks in the XRD were identified as Cu_8Zr_3, CuTiZr, and Pd_3Zr. There were also noticed minor amounts of the PdTi phase and MTi_2-type phases (M = Cu, Zr). The identified phases are marked in Fig. 8. For the Cu_8Zr_3 orthorhombic phase, the lattice parameters were determined to be $a = 0.8147$, $b = 0.824$, $c = 0.997$ nm and for the tetragonal cell of the CuTiZr phase $a = 0.306$ and $c = 1.10$ nm. The Pd_3Zr tetragonal phase with fcc structure had lattice parameters $a = 0.562$ and $c = 0.923$ nm (Table 2).

Table 1 Comparison of the characteristic temperatures of transformations, heating rate 30 °C/min, T_g—glass transition temperature, $\Delta T = T_x - T_g$, T_x—peak onset point, T_m—melting temperature, T_L—liquidus temperature, GFA—glass forming ability

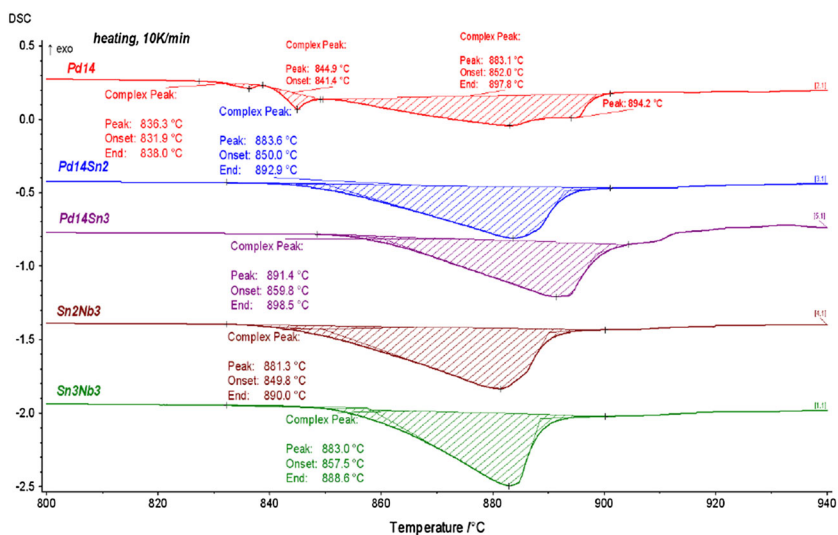| Alloy (rod φ3 mm)	Characteristic temperatures, °C (onset point meth.)						
	T_g	T_x	ΔT	T_m	T_L	$T_L - T_m$	GFA
Pd-14	404	450	47	832	897	65	0.391
Sn-2	411	466	55	850	892	42	0.400
Sn-3	413	472	59	860	899	39	0.409
Sn-2Nb-3	406	455	49	850	890	40	0.395
Sn-3Nb-3	407	467	60	858	889	31	0.402

Fig. 5 Comparison of the DSC curves presenting melting of the investigated alloys; heating rate 10 °C/min
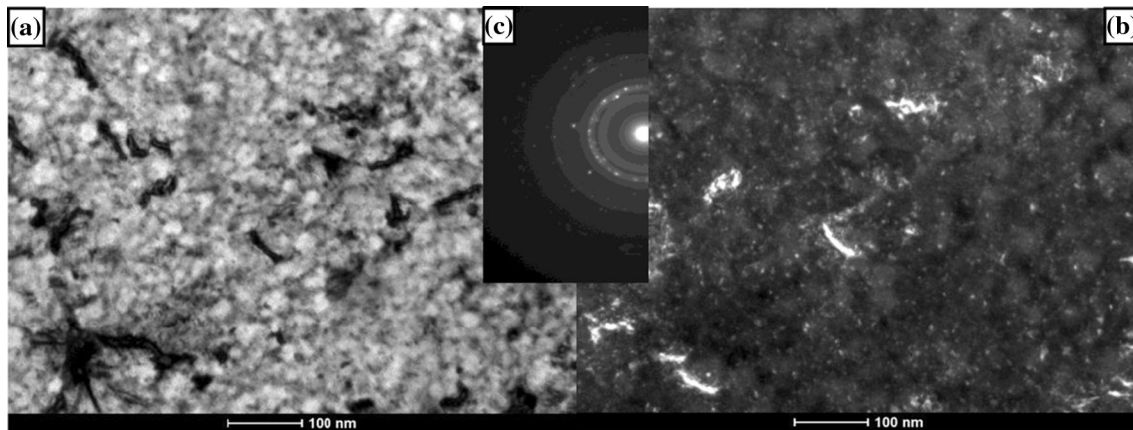

Fig. 6 TEM microstructure of (Sn-2) sample annealed at 455 °C: (a) bright-field (BF), (b) dark-field (DF), and (c) selected area electron diffraction (SAED) pattern

The multi-phase Rietveld analysis was used for the determination of the volume fractions of the three dominating phases. The possible small amounts of Ti-rich phases were ignored in calculations. Due to this analysis, the volume fraction of the Cu_8Zr_3 phase increases with the increasing content of Sn from 61 to 72 vol.%, whereas the volume fraction of the CuTiZr phase decreases from about 40 to 30 vol.%. Samples containing Sn and Nb show the same volume fractions of the Pd_3Zr phase (Table 2). Comparing above results with the phase composition of the Pd-14 alloy, it may be concluded that

the additions of Sn and Nb increase the proportion of the Cu_8Zr_3 to CuTiZr phase from nearly 1 to about 3. The Pd_3Zr phase content is just slightly decreased (Table 2).

3.4 Nanohardness of the Alloys

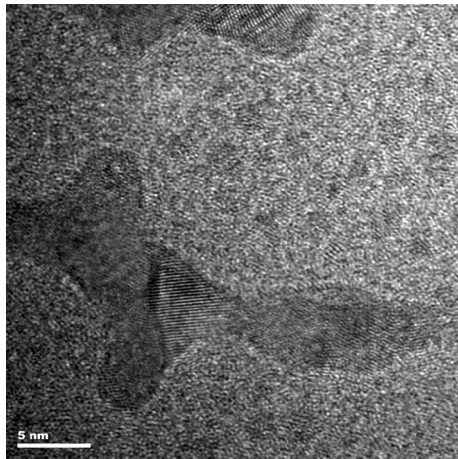Good mechanical properties of the amorphous alloys are essential for their application (Ref 11). Table 3 and Fig. 9

Fig. 7 HREM microstructure of (Sn-2) sample annealed at 455 °C

present the results of the nanohardness tests for the amorphous and fully crystalline alloys. The size of the samples used for the tests was 3.0 mm in diameter and 5 mm in height. The amorphous structure of the bulk samples for the hardness tests was confirmed separately by XRD. The nanohardness of the amorphous samples Pd-14 and Sn-3 was approximately 11 GPa and the elastic modulus 180 GPa, both values decreasing for the Sn-2 alloy but in the range of experimental error. The values of NH_V and E modulus were similar for the amorphous Sn-2Nb-3 sample but increased in case of the Sn-3Nb-3 amorphous alloy containing 1 at.% more Sn (Table 3; Fig. 9). Samples' nanohardness and elastic modulus after crystallization (Table 3; Fig. 9) remained the same in case of the Pd-14, Sn-2Nb-3, and Sn-3-Nb-3 alloys, about 16 GPa and 270 GPa, respectively, slightly lowered for the Sn-2 and clearly increased for the Sn-3 alloys.

Figure 10 shows SEM micrographs of the indentation marks for the Pd-14 (a-c) and Sn-2 (d-f) BMGs with the load increasing from 20 to 50 mN and the indentation rate changing from 0.08 to 2.0 mN/s. The difference in the indents' sizes caused by an increase of the load is noticeable as well as the ripples resulting from the pile-up of the shear bands around each indent in the amorphous phase. The number of the pile-ups increases with increasing loading rate but is smaller for the Sn-2 alloy. As the number of pile-ups indirectly reflects the number of shear bands formed, it may be concluded that the number of the shear bands increased with the increase of the loading rate (Ref 16) and was lower for the softer alloy Sn-2
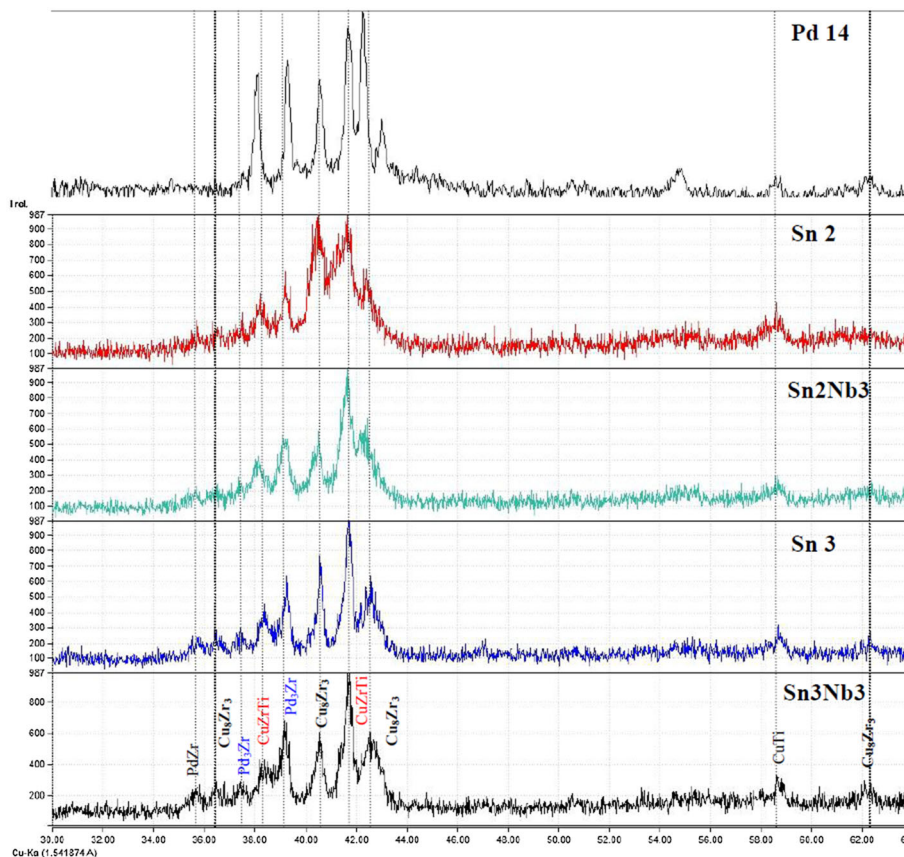

Fig. 8 XRD patterns after crystallization: (Pd-14) $Ti_{40}Cu_{36}Zr_{10}Pd_{14}$, (Sn-2) $Ti_{40}Cu_{34}Zr_{10}Pd_{14}Sn_2$, (Sn-3) $Ti_{40}Cu_{33}Zr_{10}Pd_{14}Sn_3$, (Sn-2Nb-3) $(Ti_{40}Cu_{34}Zr_{10}Pd_{14}Sn_2)_{97}Nb_3$, and (Sn-3Nb-3) $(Ti_{40}Cu_{33}Zr_{10}Pd_{14}Sn_3)_{97}Nb_3$

Table 2 Volume fraction and crystal parameters of the phases after crystallization of the samples, calculated by the multi-phase Rietveld analysis

Sample	Cu₈Zr₃ Volume fraction, %	Space group	Unit cell	CuZrTi Volume fraction, %	Space group	Unit cell	Pd₃Zr Volume fraction, %	Space group	Unit cell
Pd-14	50	Pnma	$a = 0.786$ nm	45	14/mmm	$a = 0.306$ nm	5	P63/mmc	$a = 0.562$ nm
Sn-2	61		$b = 0.824$ nm	36		$c = 1.10$ nm	3		$c = 0.923$ nm
Sn-3	72		$c = 0.997$ nm	26			2		
Sn-2Nb-3	75			23			2		
Sn-3Nb-3	63			35			2		

Table 3 Comparison of the nanohardness and elastic modulus of the amorphous and crystalline samples Pd-14, Sn-2, and Sn-3 under a load of 20 mN

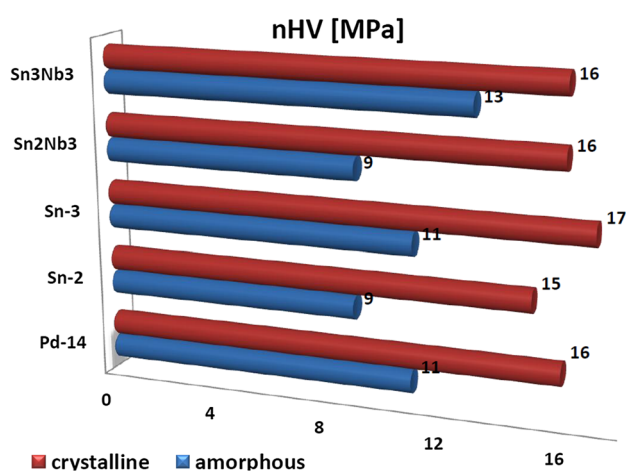| BMG	Amorphous, GPa NH$_V$ (20 mN)	E (20 mN)	Crystalline, GPa NH$_V$ (20 mN)	E (20 mN)
Pd-14	11.35 ± 1.2	178 ± 19	15.59 ± 1.6	270 ± 30
Sn-2	9.35 ± 1.6	141 ± 25	14.48 ± 1.6	265 ± 45
Sn-3	11.25 ± 1.4	175 ± 25	17.08 ± 1.7	282 ± 43
Sn-2Nb-3	9.00 ± 1.6	138 ± 25	15.50 ± 1.1	270 ± 36
Sn-3Nb-3	12.60 ± 1.2	183 ± 21	16.20 ± 1.2	273 ± 32

Fig. 9 Comparison of the NH$_V$ histogram for the bulk amorphous samples and crystalline samples of different compositions

(Table 3), also revealing a larger size of the indentation marks (Fig. 10d-f) which agrees well with the lower nanohardness measured (Table 3; Fig. 9).

4. Summary

The XRD investigations of the amorphous phase suggest an increased tendency for the formation of crystals quenched in from the liquid phase in case of the composition containing 3 at.% Sn and Nb additions. This was however not confirmed by the TEM observations and may concern a very small amount of the particles or surface oxides. What was shown by the TEM and HAADF-STEM methods was amorphous phase separation in the liquid state. The HAADF-STEM phase composition

analysis revealed that the segregation of the components does not concern Sn and Nb additions. Similar amorphous phase separation was observed earlier in case of the amorphous alloy of the composition Pd-10 (Ref 10). From the results of DSC analysis, increasing the Sn addition further increases glass transition T_g, primary crystallization T_x, melting T_m, and liquidus T_L temperatures. As a result, supercooled liquid range ΔT largely increases while the GFA increases slightly. Further Nb addition decreased all temperatures T_g, T_x, T_m, and T_L as well as ΔT and GFA parameters, but preserved tendency for their increased values for the larger 3 at.% Sn additions. This suggests independent influence of both types of atoms on the thermophysical properties of the amorphous phase of the investigated alloys. The decrease of GFA together with the Nb additions is in agreement with literature (Ref 11); however, the strong tendency for the presence of the quenched-in crystalline particles in the amorphous phase in case of the (Ti-CuZrPd)$_{100-x}$Nb$_x$ amorphous alloys was not confirmed (Ref 11). It may be assumed that the small Sn additions increasing GFA decrease clustering and nano-crystallization proceeding together with the solidification of the amorphous phase. As was shown by the isothermal nano-crystallization at T_g temperature, two separated slightly different amorphous phase compositions existed, one partially crystallized and the other remained amorphous. Cu₈Zr₂, one of the three main crystalline phases identified after crystallization from the amorphous phase, is well confirmed in literature (Ref 6). The phases identified in this paper as ternary CuTiZr and Pd₃Zr were not mentioned in the literature, but the binary phase CuTi was observed (Ref 6). From the Rietveld analysis, it may be concluded that the Sn and Nb additions do not influence the Pd₃Zr phase stability but increase the amount of Cu₈Zr₃ phase on the cost of the content of CuTiZr phase.

The amorphous phase nanohardness and elastic modulus E were decreased with the Sn 2 at.% addition by 2 GPa and 40 GPa, respectively, and were not influenced by further Nb
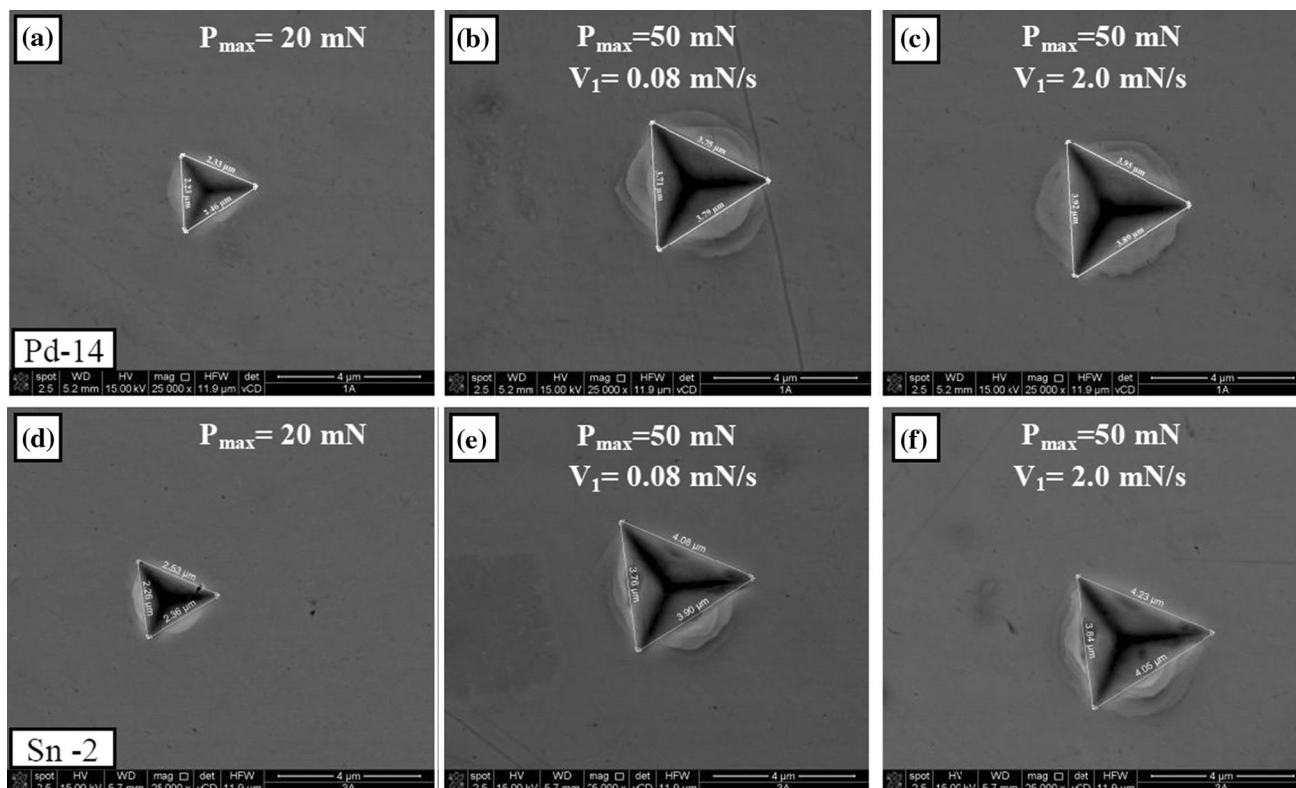
Fig. 10 SEM micrographs of the indents of the BMG Pd-14 (a) and Sn-2 (d) under 20 mN load and Pd-14 (b, c) and Sn-2 (e, f) under 50 mN load; two different loading rates of 0.08 and 2.0 mN/s, respectively

addition. In contrast, 3 at.% Nb addition to the Sn-3 alloy slightly influenced both nanohardness and elastic modulus E. The nanohardness and elastic modulus of all the samples increased after crystallization. As in the amorphous alloy, the addition of 2 at.% Sn caused a decrease of the nanohardness of the Sn-2 alloy in comparison with the Pd-14 alloy, while 3 at.% addition of Sn increased it, in both cases by about 1 GPa. It should be noticed however that Sn-2 alloy retained after crystallization a meaningful amount of the amorphous phase.

5. Conclusions

- Similarly to the previously observed amorphous phase separation in the case of the $Ti_{40}Cu_{36}Zr_{10}Pd_{10}$ alloy, in case of the alloys containing Sn or Sn and Nb additions two slightly different amorphous phase compositions were observed. The composition modifications may be presented by the formula $[(TiPd)_{50-x}(CuZr)_{50+x}]_{97}(Sn,Nb)_3$.
- Small 2 and 3 at.% additions of Sn to the $Ti_{40-}Cu_{36-x}Zr_{10}Pd_{14}Sn_x$ amorphous alloy increased glass transition (T_g), primary crystallization (T_x), melting, and liquidus temperatures as well as supercooled liquid range and GFA.
- The nanohardness and elastic modulus decreased with the 2 at.% Sn addition and for the alloy with the 3 at.% addition of Sn remained similar to characterizing Pd-14 amorphous phase.
- The 3 at.% Nb additions to the Sn-containing amorphous alloys decreased T_g, T_x, T_L, and T_m temperatures as well

as ΔT and GFA, however preserved larger values for the 3 at.% Sn-containing amorphous alloy.
- The Rietveld analysis shows that the Sn and Nb additions do not influence Pd_3Zr phase stability but increases the amount of Cu_8Zr_3 phase on the cost of the content of Cu-TiZr phase.
- It was not confirmed that small Nb additions to $Ti_{40-}Cu_{36-x}Zr_{10}Pd_{14}Sn_x$ alloys led to the noticeable amount of the quenched-in crystalline particles or crystallized phases at least of the micrometric dimensions.

Open Access

References

1. A. Inoue and A. Takeuchi, Recent Progress in Bulk Glassy Alloys, *Mater. Trans.*, 2002, **43**(8), p 1892–1906

2. M. Niinomi, Mechanical Properties of Biomedical Titanium Alloys, *Mater. Sci. Eng. A*, 1998, **243**, p 231–236

3. D. Kuroda, M. Niinomi, M. Morinaga, Y. Kato, and T. Yashiro, Design and Mechanical Properties of New β Type Titanium Alloys for Implant Materials, *Mater. Sci. Eng. A*, 1998, **A243**, p 244–249

4. A. Cremasco, W.R. Osoria, C.M.A. Freire, A. Garcia, and R. Caram, Electrochemical Corrosion Behavior of a Ti-35Nb Alloy for Medical Prostheses, *Electrochem. Acta*, 2008, **53**, p 4867–4874

5. S.L. Zhu, X.M. Wang, and A. Inoue, Glass-Forming Ability and Mechanical Properties of Ti-Based Bulk Alloys with Large Diameters of up to 1 cm, *Intermetallics*, 2008, **16**, p 1031–1035

6. S. Zhu, G. Xie, F. Qin, X. Wang, and A. Inoue, Effect of Minor Sn Additions on the Formation and Properties of TiCu ZrPd Bulk Glassy Alloy, *Mater. Trans.*, 2012, **53**, p 500–503

7. S.L. Zhu, X.M. Wang, F.X. Qin, and A. Inoue, A New Ti-Based Bulk Glassy Alloy with Potential for Biomedical Application, *Mater. Sci. Eng A*, 2007, **459**, p 233–237

8. S.L. Zhu, X.M. Wang, F.X. Qin, M. Yoshimura, and A. Inoue, New TiZrCuPd Quaternary Bulk Glassy Alloys with Potential of Biomedical Applications, *Mater. Trans.*, 2007, **48**, p 2445–2448

9. S.L. Zhu, X.M. Wang, G.Q. Xie, F.X. Qin, M. Yoshimura, and A. Inoue, Formation of Ti-Based Bulk Glassy Alloy/Hydroxyapatite Composite, *Scr. Mater.*, 2008, **58**, p 287–290

10. A. Sypien, T. Czeppe, G. Garzel, L. Litynska, J. Latuch, and N.Q. Chinh, Thermal Stability and Mechanical Properties of the TiCuZrPd Glasses with 10, 14, 20 at.%Pd, *J Alloys Compd.*, 2014, **615**, p 108–112

11. F.X. Qin, X.M. Wang, G.Q. Xie, and A. Inoue, Distinct Plastic Strain of Ni-Free Ti-Zr-Cu-Pd-Nb Bulk Metallic Glasses with Potential for Biomedical Applications, *Intermetallics*, 2008, **16**, p 1026–1030

12. E.S. Park and D.H. Kim, Phase Separation and Enhancement of Plasticity in Cu-Zr-Al-Y Bulk Metallic Glasses, *Act. Mater.*, 2006, **54**, p 2597–2604

13. G. He, J. Eckert, W. Loser, and I. Schultz, Novel Ti-Base Nanostructure-Dendrite Composite With Enhanced Plasticity, *Nat. Mater.*, 2003, **2**, p 33–37

14. A. Sypien, Observation of the Complex Local Crystallization Process in Ti-Zr-Cu-Pd Amorphous Ribbons and Bulk Metallic Glass, *Arch. Metall. Mater.*, 2013, **58**, p 347–350

15. A. Sypien and W. Przybylo, Preparation of Ti–Ni–Fe Phase by Levitation and Its Structural Characterization, *J. Mater. Sci. Technol.*, 2010, **26**, p 31–35

16. C.A. Schuh and T.G. Nieh, A Nanoindentation Study of Serrated Flow in Bulk Metallic Glasses, *Acta Mater.*, 2003, **51**, p 87–99